



# Basalt Chronology of the Orientale Basin Based on CE-2 CCD Imaging and Implications for Lunar Basin Volcanism

Jingwen Liu <sup>1,2</sup> , Jianzhong Liu <sup>1,3,\*</sup>, Juntao Wang <sup>1,3</sup>, Kai Zhu <sup>1,3</sup> and Li Zhang <sup>1</sup>

<sup>1</sup> Center for Lunar and Planetary Sciences, Institute of Geochemistry, Chinese Academy of Sciences, Guiyang 550081, China; liujingwen@mail.gyig.ac.cn (J.L.); wangjuntao@mail.gyig.ac.cn (J.W.); zhukai@mail.gyig.ac.cn (K.Z.); zhangli@mail.gyig.ac.cn (L.Z.)

<sup>2</sup> University of Chinese Academy of Sciences, Beijing 100049, China

<sup>3</sup> Center for Excellence in Comparative Planetology, Chinese Academy of Sciences, Hefei 230026, China

\* Correspondence: liujianzhong@mail.gyig.ac.cn; Tel.: +86-137-1861-1998

**Abstract:** The specific duration between the impact event and subsequent volcanic flows is highly variable based on previous works. The method of crater size-frequency distribution (CSFD) has been previously used to date the basalt in Orientale Basin, which yielded inconsistent resultant Absolute Model Age (AMA) ranges. The inconsistency may be attributed to the choice of counting area and identified superposed craters. In this study, we integrated the Chang'E-2 (CE-2) imaging data (7 m/pix) and the IIM and 20 m CE-2 DTMS data, re-divided Mare Orientale, and re-estimated the age of the basalts there. The ages revealed that (1) the central basalts had multiphase eruptions, beginning at 3.77 Ga (30 My after the impact event) with the longest duration of 1.51 Gy; (2) the edge basalts have a similar features as the central basalts, beginning at 3.75–3.50 Ga (50–300 My after the impact) with the longest duration of 0.67 Gy. Compared with the basalts along the basinal margin, the central basalts have higher Ti but lower Mg<sup>#</sup> contents, consistent with the basaltic magma fractionation trend. Spatial distribution characteristics indicate that the basalt eruption occurred in the impact direction upstream and in the center, but almost absent in the impact direction downstream. Accordingly, we speculate that the longevity of the lunar mare basaltic volcanism was affected by gravity changes, material balance, and other post-impact processes.

**Keywords:** CE-2 CCD image; Orientale Basin; Absolute Model Age (AMA); volcanic formation



**Citation:** Liu, J.; Liu, J.; Wang, J.; Zhu, K.; Zhang, L. Basalt Chronology of the Orientale Basin Based on CE-2 CCD Imaging and Implications for Lunar Basin Volcanism. *Remote Sens.* **2022**, *14*, 1426. <https://doi.org/10.3390/rs14061426>

Academic Editors: Christian Wöhler, Kaichang Di, Long Xiao and Jessica Flahaut

Received: 13 January 2022

Accepted: 8 March 2022

Published: 15 March 2022

**Publisher's Note:** MDPI stays neutral with regard to jurisdictional claims in published maps and institutional affiliations.



**Copyright:** © 2022 by the authors. Licensee MDPI, Basel, Switzerland. This article is an open access article distributed under the terms and conditions of the Creative Commons Attribution (CC BY) license (<https://creativecommons.org/licenses/by/4.0/>).

## 1. Introduction

Lunar volcanic history is a key to understanding lunar thermal evolution [1]. After the formation of the Moon at ~4.5 Ga [2], melt in the lunar magma ocean resided in the lunar mantle and affected the duration of lunar volcanism, according to the lunar thermal evolution model [3]. The Mg-rich cumulates at the bottom of the lunar mantle (formed in the early magma ocean period) are less dense than the Ti-rich cumulates at the top (formed in the late magma ocean period) and the original KREEP (potassium (K), rare earth elements (REE), and phosphorus (P)) layer [1]. With later geological influence, the gravitational imbalance between the Mg-/Ti-rich cumulates may have caused the primitive lunar mantle to overturn. The accompanied decompression melting may have formed the lunar mare basaltic volcanism [4,5], which constituted the main endogenic dynamics of the Moon. Lunar mare basalts, although accounting for only a very minor proportion of the lunar crust (1%), their petrogenesis and temporal-spatial distribution have recorded the geochemistry and evolution of the lunar mantle reservoir.

Because most lunar mare basalts are still unsampled, absolute radiometric age data for the majority of basalts are still lacking. Fortunately, by making use of remote sensing techniques, we can derive relative and absolute model ages for these unsampled regions [6–9]. Hiesinger et al. [6–9] performed Crater Size-Frequency Distribution (CSFD) measurement on many Procellarum KREEP Terrane (PKT) maria using Lunar Orbiter

images (50–150 m/pix), with the counting crater diameter ranging between 1 and 10 km. Morota et al. [10], Lucey, P.G. et al. [11] used the SELENE (Kaguya) (10 m/pixel) to estimate the age of the main stratigraphic units in the lunar PKT area, using two CSFD statistical dating methods and craters of 250 m diameter. Pasckert [12] utilized the Lunar Reconnaissance Orbiter Camera (LROC) Wide-Angle Camera images (WAC) (108 m/pix) to divide the basalts in/around the South Pole-Aitken basin and the CSFD to estimate the age, using craters of 1 km diameter. These CSFD results and limited basalt samples collected by the Apollo, Luna, and CE-5 missions indicate that lunar volcanism may have been active for almost 3 Gy, starting at 3.9–4.0 Ga and ceasing at 1.2 Ga ago, with most basalts erupting in the late Imbrian period (3.6–3.8 Ga) [6,13]. The prolonged eruption and compositional heterogeneity of the lunar basalts imply compositional heterogeneity of the lunar interior. The lunar basalts can thus reveal the lunar interior composition, source region, and thermal evolution.

A total of 17% of the lunar surface is covered by 23 lunar maria [14], lying within or adjacent to large impact basins. Most of the lunar maria (20 out of 23) are located in the PKT, and the remaining three (i.e., Mare Orientale, Mare Moscoviense, and Mare Ingenii) are located in the highlands [15]. Almost all maria belong to impact basins, generally distributed in the center of the basins, which is a large basalt area in the center of a basin. However, not all basins have basalt, and not all basalt areas in the center of the basin can be defined as the mare, only the deposits of basaltic composition (i.e., mafic impact melts) in the center of basins can be defined as mare materials.

As shown in Figure 1: (1) In and near the PKT, basalt filled more than two annular structural regions or even all basins, the diameter of basins ranging from 100+ km (e.g., Iridum Basin) to 1000 km (e.g., Serenitatis Basin); (2) In the transition zones between the PKT and highland, and South Pole-Aitken Terrian (SPAT), some other basins only have basalts in the center and margin, distributed, with a diameter spanning from 100+ km (e.g., Schrödinger Basin) to 1000 km (e.g., Orientale Basin); (3) Some basins are exceptions, such as Austral Basin, but it is all filled with basalt.

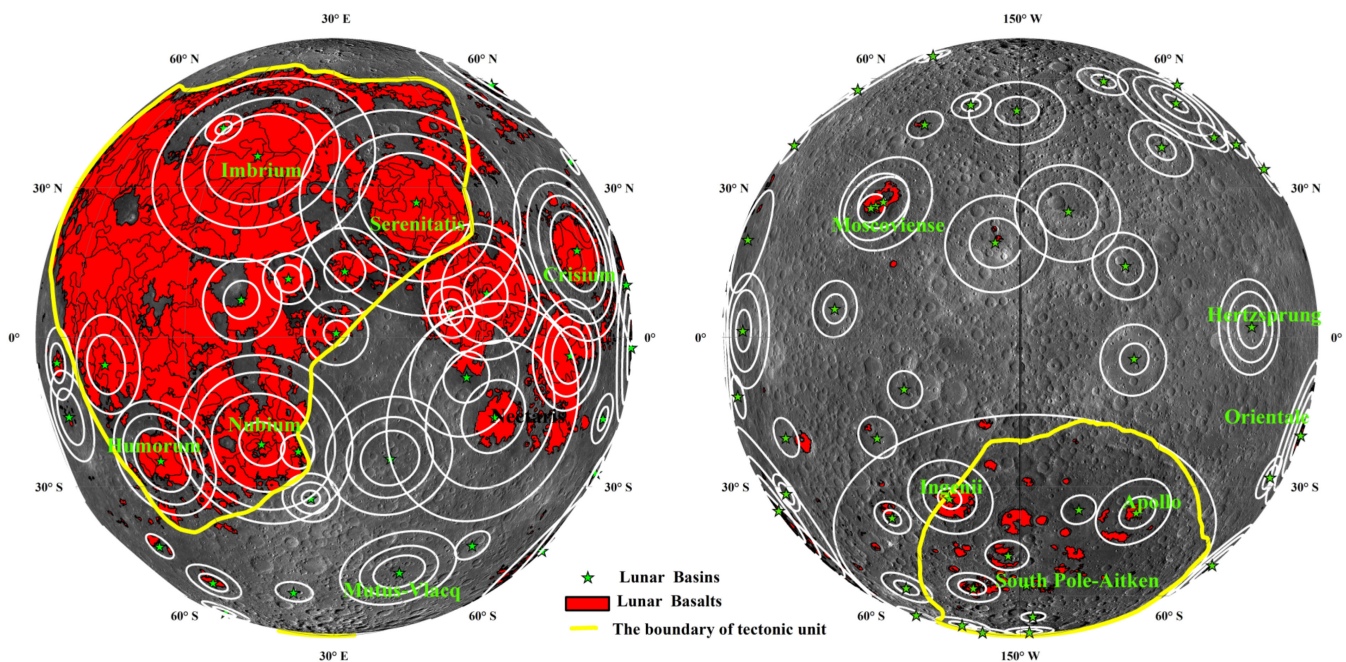


**Figure 1.** Distribution of the lunar basalts and basins in WAC image (108 m/pix). The boundary of the technical unit based on the work of Jolliff et al., [16], the rings the basins based on the work of Liu et al. [17]; the boundary line of basalt based on the work of Hiesinger et al. [6–9], Morota et al. [10], and Pasckert et al. [12].

Basin impact events are the major exogenic geological process on the Moon during 3.8–4.3 Ga. Exploring the interrelationship between the lunar basalt and basins is the key to uncovering the connection between lunar exogenic and endogenic geological processes. Lunar volcanism did not begin immediately after the basin-forming impacts [18], which implies that the impacts did not directly trigger the volcanism [19], yet their close spatial link implies some sort of genetic connection. To determine any potential interrelationship between them, the following questions need to be answered: (1) the timing of mare volcanism in/around the basin, and any migration of volcanism with time; (2) the possible cause of age difference (if exists) between the basalts and the impact event(s); (3) any spatial distribution trend (and the cause of it) of basalts in the basin.

The multi-ring Orientale Basin, which is locally filled with mare basalts, offers an opportunity to answer these questions. By studying the age and geological characteristics of the Mare Orientale basalts, the relationship between mare basaltic volcanism and the basin formation can be readily established [20]. Although the region has not been sampled, the method of crater size–frequency distribution (CSFD) has been used to date the eruption age of basalts in previous studies. Unfortunately, the resultant Absolute Model Age (AMA) ranges inconsistency, which hinders understanding of the relationship between basins and subsequent volcanic flows after impact. The inconsistency may be attributed to the choice of counting area and identified superposed craters. In this study, we investigate the described discrepancy in AMAs between mare basalts in/around the Orientale basin Chang'E series data. In addition, the element compositions and impact direction are combined to reveal the relationship between the basin volcanism and impact events, which provides new ideas for explaining the age differences.

## 2. Orientale Basin

The Orientale Basin is the youngest and best-preserved multi-ring lunar impact basin and has only undergone mild modification by subsequent minor impacts and volcanism [21]. The basin is scientifically interesting since its interior remains largely unobscured by mare deposits (unlike most other prominent nearside basins [22]) and allows investigation of an early-filling mare stage.

The circular Orientale Basin was formed in the Imbrian period and has four ring structures, with diameter of approximately 313, 520, 615, and 919 km based on the Lunar Orbiter Laser Altimeter (LOLA) data (Figure 2a). The AMA of the Orientale Basin was estimated to be 3.8 Ga [23], with 38 craters mapped (a few 20 km in diameter) on the Orientale Basin ejecta [24]. Similar work by Baldwin [25] yielded an AMA of ~3.79 Ga. Recently, Yue et al. [21] reported a AMA of ~3.80 Ga for the Orientale Basin, using craters of 0.7 km diameter in the entire ejecta around the basin.

After the basin formation, lava erupted and deposited locally in the basin, forming basalt units in its center and rim: (1) Mare Orientale, the basalt areas in the center of Orientale Basin; (2) Lacus Veris, the basalt areas between the Inner Rook Ring and the Outer Rook Ring; (3) Lacus Autumni, the basalt areas between the Outer Rook Ring and Cordillera Ring [26] (Figure 2b). However, there are certain deviations in the division of geological units and age statistics of basalts in this area, as shown in Table 1 and Figure S1.

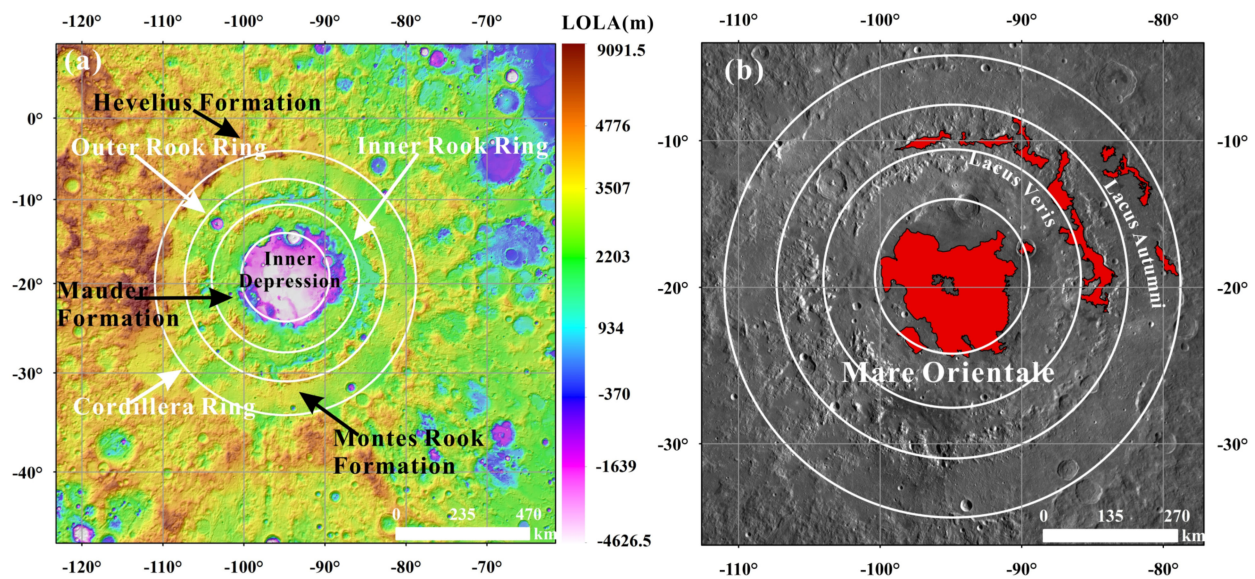


**Figure 2.** (a) Location map of Orientale Basin with four main rings (the rings the basins based on the work of Liu et al. [17]) and deposits labeled (the deposits based on the work of Whitten et al. [20]) in LOLA data; (b) The lunar basalts (the basalts based on the work of Morota et al. [10]) of the Orientale Basin in WAC image (108 m/pix).

**Table 1.** The AMAs ages of basalts in the Orientale Basin.

Basalts Name	Reference	Subunit Name	The surface Age of Basalts (Ga)
Mare Orientale	Greely et al., 1993 [27]	Mare Orientale West (1)	3.45
		Mare Orientale Southeast (2)	3.45
		Mare Orientale South-Central (3)	3.70
	Cho et al., 2011 [28]	Southwest	3.77
		SW Polygon	3.77
east		2.91	
Whitten et al., 2011 [20]	Mare sheet	3.64	
	Mare Orientale 7 Kopff	3.57 3.36	
Lacus Veris	Greely et al., 1993 [27]	Lacus Veris	2.85
	Cho et al., 2011 [28]	Noth	2.16, 3.36, 3.56
		South	2.20
	Whitten et al., 2011 [20]	9	3.44
		11	3.22
12		3.36	
14		3.20	
Lacus Autumni	Greely et al., 1993 [27]	Lacus Autumni	3.85
	Cho et al., 2011 [28]	North	2.03
		Middle	1.75
		South	2.16
	Whitten et al., 2011 [20]	21	3.47
22		1.66	
23		2.38	

### 3. Data and Methods

#### 3.1. Crater Size-Frequency Distribution (CSFD) Model

CSFD measurement is a powerful remote sensing technique to obtain relative age and AMA for unsampled planetary surfaces, such as the Orientale basalts. The surface area of the unit and the primary impact crater within the unit were mapped with the ArcGIS add-in “CraterTools”, which measures the unit area and the crater diameter [29]. Subsequently, the crater distributions measured on geologic units of different ages can be aligned along a complex continuous curve in CraterStats2 [30].

It is reasonable to assume that the physical properties of the target (e.g., density) can influence the crater size. However, the errors introduced by different crater sizes (due to differences in target material) are irrelevant because only the Orientale mare basalts were dated here. Secondary craters formed from the ejected material of a primary crater are thus not correlated to the impact rate, yet most secondary craters can be readily identified and excluded from the crater counts by their cluster/chain occurrence, elongated/irregular outline, and the herringbone pattern of their ejecta [31–33].

Moreover, the resurfacing of a magma eruption would preferentially cover smaller craters in the older unit, while larger craters would remain detectable. Continued impact cratering would form a new crater population in the younger unit. The selective masking of smaller craters would cause a deflection in the distribution between two segments on the age curve in the CSFD, which have different tangential isochrons [10]. The lower isochron can be used to approximate the end time of the resurfacing event (i.e., the age of surface basalt), whereas the upper isochron can be used to approximate the underlying basalt age [10]. The smaller impact craters would be destroyed by later impact craters and basalt eruption, whereas the larger impact craters would not be completely filled with basalt due to their greater depth. As a result, two or three isochrons would appear in the CSFD.

#### 3.2. Data

The CSFD measurement method is generally dependent on the data image quality, i.e., the spatial resolution and the illumination conditions, on which the crater counts are performed [9]. The datasets used here include those from CE-2 (<http://moon.bao.ac.cn/>, accessed on 15 November 2021): 20 m-resolution CE-2 DTMs (Digital Terrain Models) (ID of the data used: H005, H006, I005, I006) and 7 m-resolution CE-2 CCD images (charge-coupled-device) images (ID of the data used: H113, H114, H115, H214, H213, H212, H211, I113, I211, I212, I213, I111, I112).

Although the CE-2 CCD images (7 m/pixel, incidence angle: 5°) [34] have a higher sun-angle than the WAC (108 m/pixel, incidence angle: 60°) (Figure 3a,d), an order of magnitude better than WAC. As a result, taking three different types of the crater as an example, we can issue these three craters measurable in the CE-2 CCD images (Figure 3c) are either barely visible or saturated in the WAC image (Figure 3e), which would yield better correct crater statistics and reliable ages using CE-2 CCD images. (1) There is a crater in area “I” (diameter: 415 m). Its display is dimmer in the original 7 m-resolution CE-2 CCD image (Figure 3b), but clearly displayed in the 7 m resolution CE-2 CCD effect after partial stretching (Figure 3c). The display is the clearest when the 7 m resolution CE-2 CCD is superimposed on the 20 m resolution CE-2 DTMs (Figure 3f), but the crater is still the least visible in the WAC image even after partial stretching (Figure 3e); (2) In area “II”, a degraded crater is identified in the 7 m resolution CE-2 CCD data superimposed on the 20 m-resolution CE-2 DTMs as shown in Figure 3b,c,e,f; (3) In “III” area, small-scale impact craters, such as a 62-m impact crater, are identified on the CE-2 data (Figure 3c,f), which diameter has exceeded the size of a WAC pixel (108 m/pix).

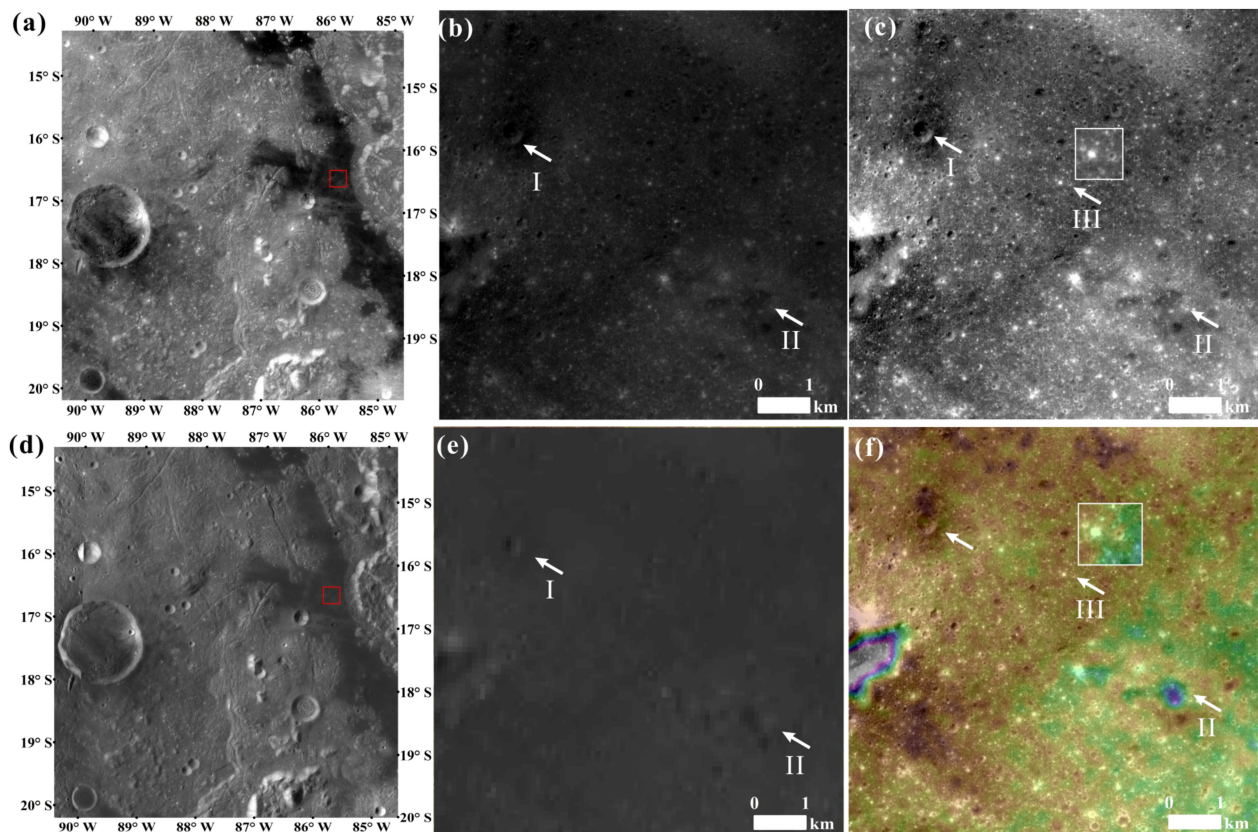


**Figure 3.** Comparison between CE-2 data with WAC data (108 m/pix): (a) 7 m resolution CE-2 CCD images of part of Orientale Basin: CE2\_GRAS\_DOM\_07m\_I112\_17S088W\_A.tif, the red box indicates the location of (b,c,e,f); (b) original 7 m resolution CE-2 CCD image of the red box area in a and d; (c) the 7 m resolution CE-2 CCD image of the red box area in a and d after partial stretching, the white box area is the enlarged image of the area indicated by the white arrow III; (d) WAC (108 m/pix) of part of Orientale Basin, the red box indicate the location of (b,c,e,f); (e) WAC image of the red box area in a and d after partial stretching; (f) the 7 m resolution CE-2 CCD data superimposed on 20 m-resolution CE-2 DTMs of the red box area in a and d, the white box area is the enlarged image of the area indicated by the white arrow III.

In summary, despite the higher sun-angle of CE-2 CCD data, the impact features with small diameters have a higher definition in CE-2 CCD images after local stretching, which is more conducive to identifying these small craters. After superimposing CE-2 DTMs on CCD data, some severely degraded craters become clearer. Therefore, these advantages of CE-2 data all would help to facilitate the crater counting and yield a more reliable AMAS in the CSFD using CE-2 data.

The  $\text{TiO}_2$  and FeO content product derived from the Chang'E-1 (CE-1) Interference Imaging Spectrometer (IIM) data with the algorithms described by Wu et al. [35] is used to evaluate the boundaries of maria basalt units in this research. The global product is released with a spatial resolution of  $\sim 200$  m/pixel. The  $\text{Mg}^\#$  are calculated by the MgO and FeO abundance from Lunar Prospector (LP) [36]

## 4. Results

### 4.1. Basaltic Area Identification

Hiesinger et al. [6] assume that the spectrally-homogenous units were formed within a relatively short period, and have first-order similarity in mineralogy, representing a single eruptive phase. However, from the  $\text{TiO}_2$  and FeO contents calculated from the Chang'E-1 Interference Imaging Spectrometer (IIM) data with the algorithms described

by Wu et al. [35] (Figure 4a,b), the basalts in the center of the Orientale Basin are not a single geological unit. Greeley et al. [27] used the Galileo SSI albedo (0.56  $\mu\text{m}$ ) image superimposed on a shaded airbrush map and divided this basalt field into four sub-regions. Nonetheless, due to the low data spatial resolution, this approach was not adopted by some subsequent studies [28,37,38]. Consequently, Mare Orientale is still regarded as a single geological unit for age calculation and other related research. Combined with the work of Greeley et al. [27], the estimated  $\text{TiO}_2$  and  $\text{FeO}$  contents, and CE-2 CCD data, we have divided the sub-geological units of Mare Orientale in greater detail (Figure 4c). Among them, (1) the positions of c1 and c9 are separated from other subunits; (2) c2 has lower  $\text{FeO}$  content and  $\text{TiO}_2$  content; (3) the  $\text{FeO}$  content and  $\text{TiO}_2$  content of c3 and c5 are both higher, but there is a transition zone between them, which is more likely to belong to two eruptions; (4) c4 has highest  $\text{FeO}$  content and  $\text{TiO}_2$  content; (5) both c6 and c8 have lower  $\text{TiO}_2$  content, but c6 has higher  $\text{FeO}$  content; (6) c7 has higher  $\text{FeO}$  content and lower  $\text{TiO}_2$  content. The boundary (white line in Figure 4c, 4d) between them can be shown in combination with CE-2 CCD images.

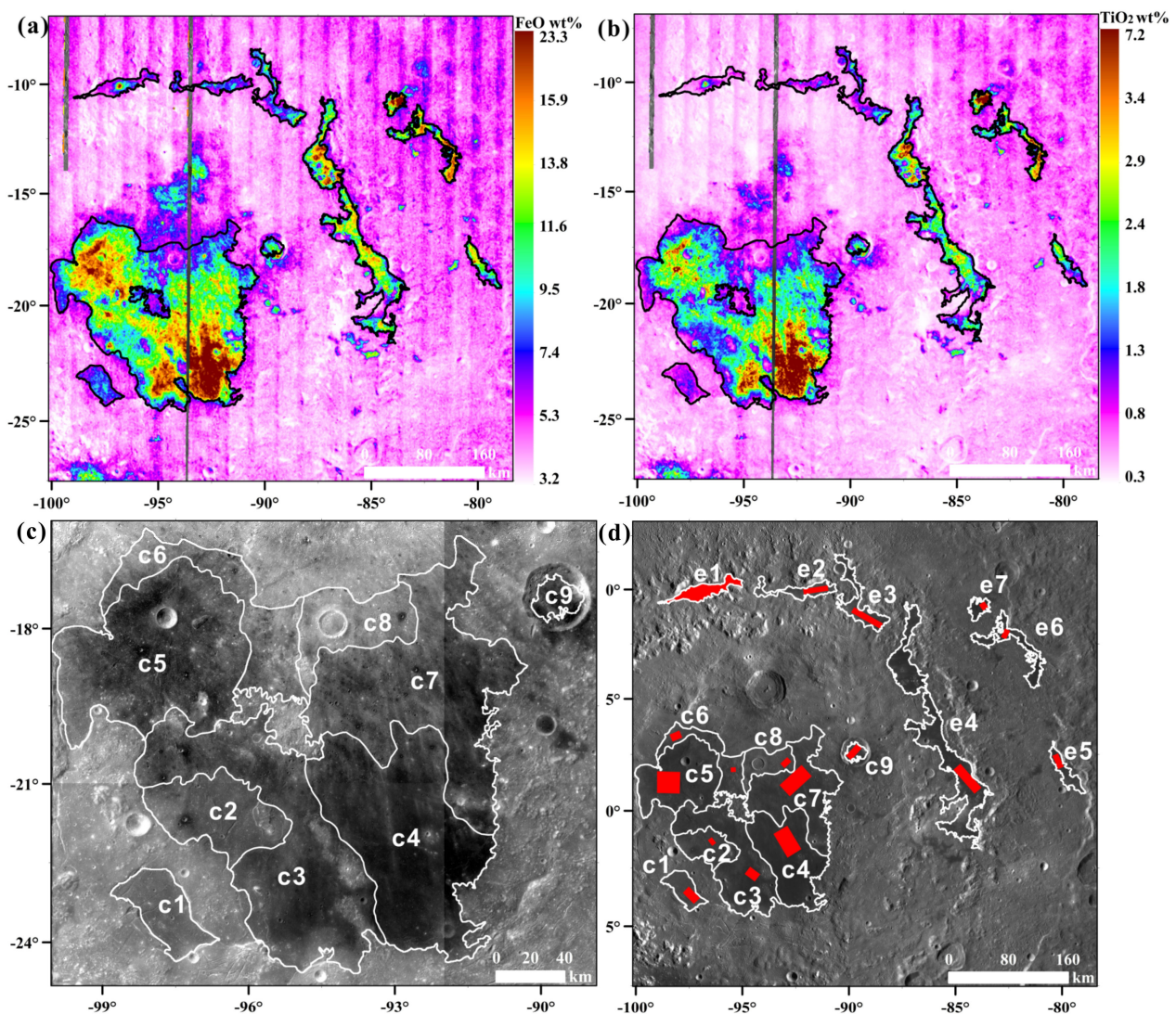


**Figure 4.** (a) IIM  $\text{FeO}$  abundance (wt%) map of the study area; (b) IIM  $\text{TiO}_2$  abundance (wt%) map of the study area; (c) Newly defined geologic (basalt) units of the Orientale Basin. White lines denote the central basalts. As the background image is spliced from 7 CE-2 CCD images, there is a slight banding; (d) Basalts and crater counting areas of this study in WAC data. Red boxes denote the crater-counting areas.

Based on the basalt distribution, Lacus Veris and Lacus Autumni are divided into four and three sub-geological units, respectively.

When calculating the age, the counting areas are located within spectrally homogenous areas of a single mapped unit. For reliable CSFD measurements, we paid particular attention to excluding areas affected by other geological events, endogenic and secondary craters (Figure 4d).

#### 4.2. Crater Retention Ages

In total, 16,823 craters (0.06 km diameter) were mapped in the Orientale Basin basalts. The mapped crater dataset and their information are given in the supplementary material (the craters counted in the different areas.scc). In contrast, the smaller craters (0.2 km diameter) are only partially recognized, with the diameter-number curve flattening toward smaller diameters, inconsistent with the CSFD rule. As a result, 3296 craters (0.2 km diameter) were used here to estimate the AMAs of the Orientale Basin basalts.

As shown in Figures 5–7, the ages obtained by CSFD of subunits c2, c5, c7, c9, e3, e4, and e7, as described in Section 3.1, appear segmented. The appearance of this phenomenon indicates that there may be multiple eruptions in the basalt units of the Orientale Basin. The younger age represents the surface age of the basalts, whilst the older age represents the underlying age of basalt. Meanwhile, combined with the impact age of the Orientale Basin, the oldest of the segmented ages obtained may be the age of the first large-scale basalt eruption after the basin impact in the subunits. The results are described in detail as follows.

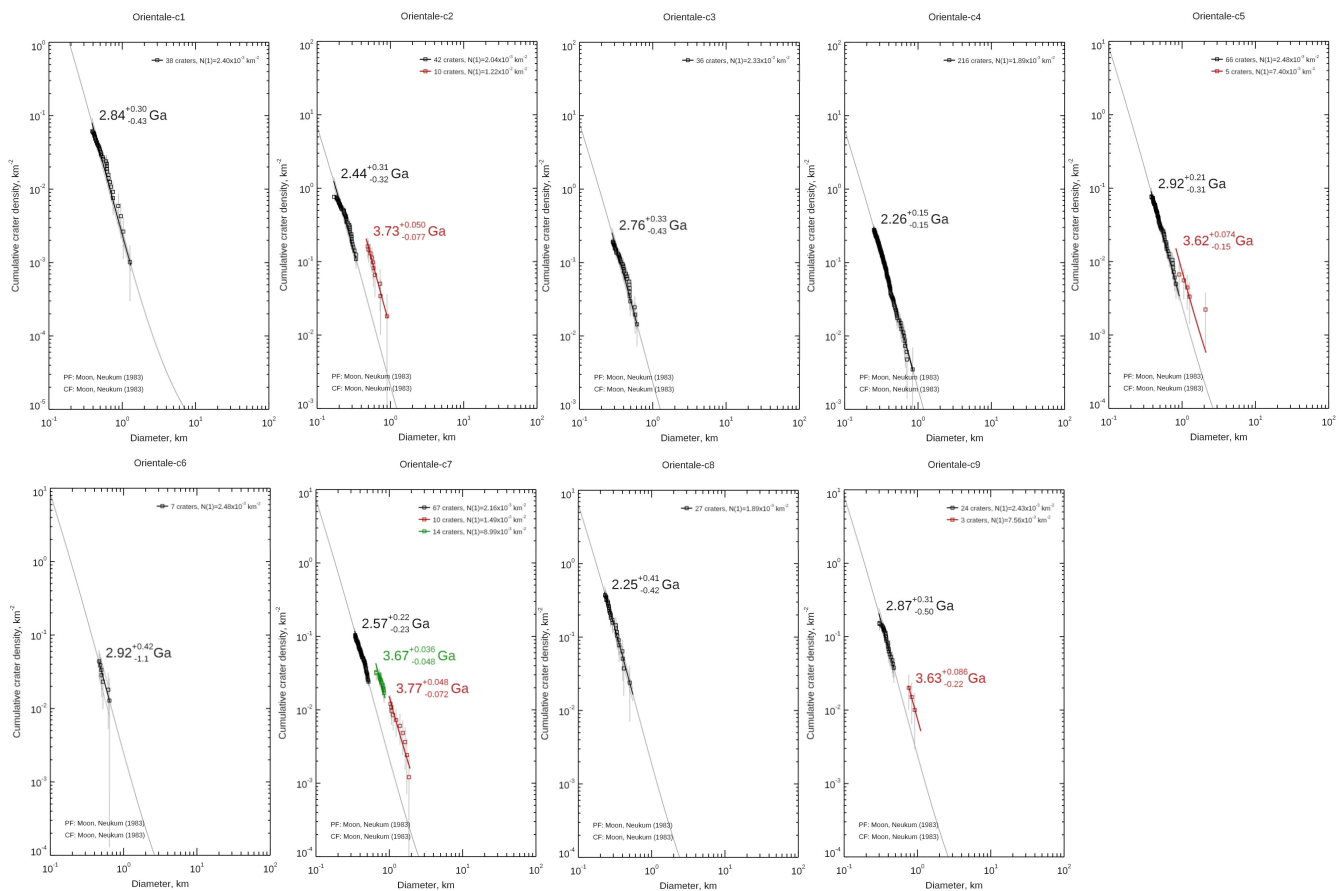


**Figure 5.** CSFD and mean AMAs of sub-units c1–c9 in Mare Orientale. Black characters denote the surface age of basalts, the red and green colors represent the older age of the underlying basalt. The AMAs were estimated with the Craterstats2 Tool with the production and chronology functions of [37].

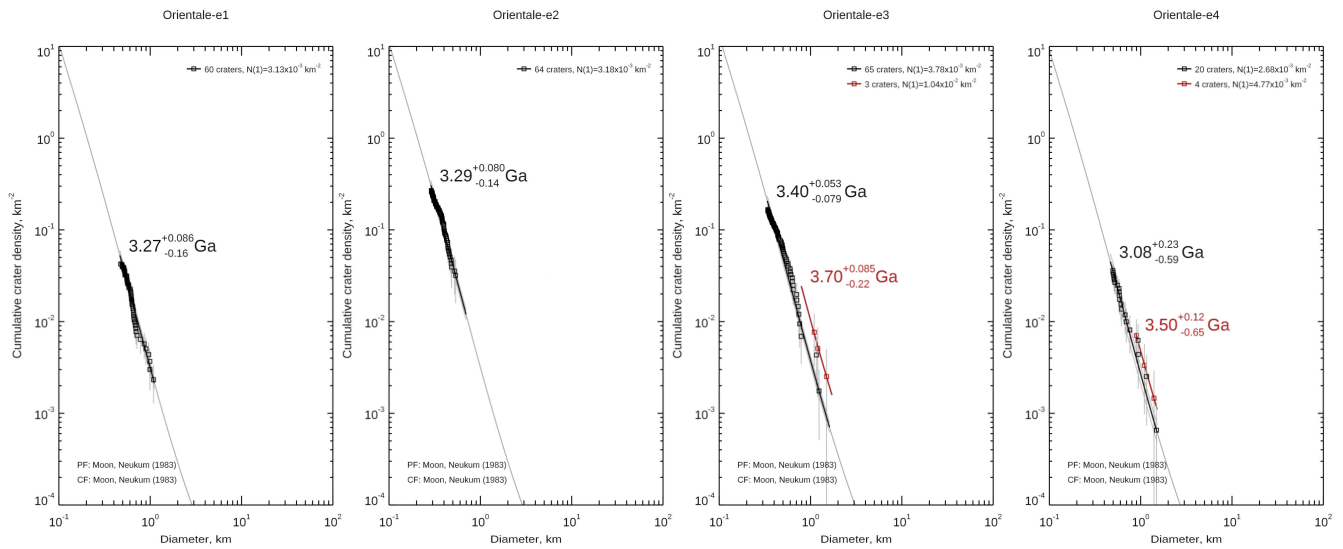


**Figure 6.** CSFD and mean AMAs of sub-units e1–e4 in Lacus Veris. Black characters denote the surface age of basalts, the red and green colors represent the older age of the underlying basalt. The AMAs were estimated with the Craterstats2 Tool with the production and chronology functions of [37].

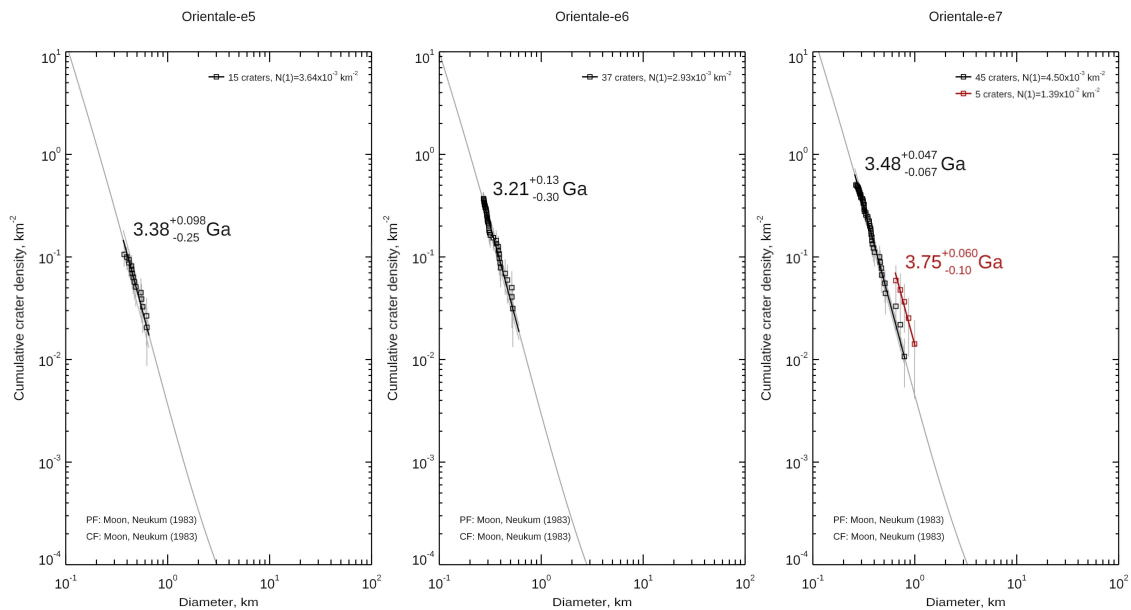


**Figure 7.** CSFD and mean AMAs of sub-units e5–e7 in Lacus Autumni. Black characters denote the surface age of basalts, the red and green represent the older age of the underlying basalt. The AMAs were estimated with the Craterstats2 Tool with the production and chronology functions of [37].

In Mare Orientale, the estimated surface ages of the nine spectrally-homogeneous central Orientale basalt units range from 2.26 to 2.92 Ga (Figure 5), which are much younger than those estimated by Greely et al. [27] and Whitten et al. [20], and slightly younger than those estimated by Cho et al. [28] (Table 2). The elimination of secondary craters made possible by the high-resolution observations may account for the younger age we obtained. Moreover, the larger craters (D 1 km) of the distribution in c2, c5, c7, and c9 lie on the older isochrons, which is simply interpreted as the AMA of the pre-existing basalt surface. These older ages are similar to the age of the basin impact event and likely represent the age of the first basalt eruption after the impact event.

**Table 2.** Model ages of the basalts in Orientale Basin.

Unite Name	Neukum et al., (1983) (Ga)		Neukum et al., (2001) (Ga)		Age of Similar Geological Units in Previous Study (Ga)
	sAMA <sup>1</sup> (Ga)	eAMA <sup>2</sup> (Ga)	sAMA (Ga)	eAMA (Ga)	
Mare Orientale					
c1	2.84 (+0.30; −0.43)	\	2.82 (+0.30; −0.43)	\	N <sup>3</sup> , 3.57 <sup>4</sup> , 3.77 <sup>5</sup>
c2	2.44 (+0.31; −0.32)	3.73 (+0.050; −0.077)	2.33 (+0.30; −0.31)	3.73 (+0.050; −0.077)	N <sup>3</sup> , 3.64 <sup>4</sup> , 3.77 <sup>5</sup>
c3	2.76 (+0.33; −0.43)	\	2.68 (+0.35; −0.42)	\	3.70 <sup>3</sup> , 3.64 <sup>4</sup> , 3.77 <sup>5</sup>
c4	2.26 (+0.15; −0.15)	\	2.18 (+0.15; −0.15)	\	3.45 <sup>3</sup> , 3.64 <sup>4</sup> , 2.91 <sup>5</sup>
c5	2.92 (+0.21; −0.31)	3.62 (+0.074; −0.15)	2.88 (+0.22; −0.31)	3.62 (+0.075; −0.16)	3.45 <sup>4</sup> , 3.64 <sup>4</sup> , 2.91 <sup>5</sup>
c6	2.92 (+0.42; −1.3)	\	2.88 (+0.45; −1.1)	\	3.45 <sup>a</sup> , 3.64 <sup>4</sup> , 2.91 <sup>5</sup>
c7	2.57 (+0.22; −0.23)	3.77 (+0.048; −0.032)	2.49 (+0.22; −0.22)	3.76 (+0.048; −0.072)	N <sup>3</sup> , 3.64 <sup>4</sup> , 2.91 <sup>5</sup>
c8	2.25 (+0.41; −0.42)	\	2.15 (+0.40; −0.40)	\	N <sup>3</sup> , 3.64 <sup>4</sup> , 2.91 <sup>5</sup>
c9	2.87 (+0.31; −0.50)	3.63 (+0.005; −0.22)	2.78 (+0.35; −0.49)	3.63 (+0.085; −0.22)	N <sup>3</sup> , 3.36 <sup>4</sup> , N <sup>5</sup>
Lacus Veris					
e1	3.27 (+0.086; −0.16)	\	3.27 (+0.086; −0.16)	\	N <sup>3</sup> , 3.44 <sup>4</sup> , N <sup>5</sup>
e2	3.29 (+0.080; −0.14)	\)	3.25 (+0.090; −0.17)	\	N <sup>3</sup> , 3.22 <sup>4</sup> , N <sup>5</sup>
e3	3.40 (+0.053; −0.079)	3.70 (+0.085; −0.22)	3.39 (+0.055; −0.083)	3.70 (+0.085; −0.22)	N <sup>3</sup> , 3.36 <sup>4</sup> , N <sup>5</sup>
e4	3.08 (+0.23; −0.59)	3.50 (+0.12; −0.65)	3.08 (+0.23; −0.59)	3.51 (+0.11; −0.60)	2.85 <sup>3</sup> , 3.20 <sup>4</sup> , 2.16, 3.36, 3.56, 2.20 <sup>5</sup>
Lacus Autumni					
e5	3.38 (+0.098; −0.25)	\	3.37 (+0.10; −0.27)	\	N <sup>3</sup> , 3.47 <sup>4</sup> , 2.03 <sup>5</sup>
e6	3.21 (+0.13; −0.30)	\	3.16 (+0.15; −0.35)	\	3.85 <sup>3</sup> , 1.66 <sup>4</sup> , 1.75 <sup>5</sup>
e7	3.48 (+0.047; −0.067)	3.75 (+0.060; −0.10)	3.46 (+0.049; −0.071)	3.76 (+0.060; −0.10)	3.85 <sup>3</sup> , 2.38 <sup>4</sup> , 2.16 <sup>5</sup>

<sup>1</sup> sAMA is the surface age of basalts; <sup>2</sup> eAMA is the oldest age of the underlying basalt. <sup>3</sup> Reference, Greely et al., (1993); <sup>4</sup> Reference Whitten et al., (2011); <sup>5</sup> Reference Cho et al., (2011).

Meanwhile, the ages calculated for the four main basalt ponds in Lacus Veris range from 3.08 to 3.40 Ga (Figure 6), consistent with previous estimates [20,27,28] (Table 2). Moreover, the larger craters (D 1 km) of the distribution in e3 and e4 lie on the older isochrons, which may represent the timing of the basalt eruption of the first phase of Lacus Veris. For Lacus Autumni, the estimated ages of the three spectrally homogeneous rim basalt units range from 3.21 to 3.48 Ga (Figure 7), which are much older than previous estimates [20,27,28] (Table 2). Partially degraded craters are identified in high-resolution images, causing older ages in these small dating sites. The larger craters (D 1 km) of the distribution in e9 lie on the older isochron, which may represent the age of the first basalt eruption at Lacus Autumni.

## 5. Discussion

### 5.1. Implications to the Volcanic History in the Orientale Region

The AMAs of basalt subunits (Figures 5–7) provide information of the volcanic history in the Orientale Region. Based on the estimated ages of mare deposits, we reconstruct the following volcanic history for the Orientale region: (1) 3.80 Ga impact occurred in the Orientale Basin [21]; (2) Basalt eruptions in Mare Orientale started soon after the impact (3.77 Ga); (3) Large part of basalts in the basin center was last resurfaced at 2.26 Ga, with an age difference of 1.5 Gy; (4) Lacus Veris may have erupted during 3.70–3.50 Ga, but the latest eruption occurred at 3.08 Ga after an interval of 0.62 Gy; (5) Lacus Autumni erupted at 3.75 Ga, and ceased to erupt at 3.21 to 3.48 Ga (~0.4 Ga after the eruption).

We suggest that the mare volcanism was first focused in the basin center, and then occurred in the basin margin. However, due to some unknown mechanisms, the volcanism in the center lasted longer, resulting in a younger surface age.

### 5.2. Implications for the Basin Volcanism

#### 5.2.1. $\text{TiO}_2$ and $\text{Mg}^\#$ Contents of the Orientale Basalts

Although global remote sensing data indicate no simple relationship between the Ti content and the mare basalt age, and that basalts with varying Ti content could have erupted coevally [39–41]. Therefore, Ti content cannot be used as a research indicator when studying the eruption characteristics of global lunar basalts. However, remote sensing data also revealed that the basin-scale mare volcanism evolved independently of neighboring regions [42], a possible relationship between Ti content and volcanic age has been reported in every separate basin [42]. The wide Ti range of mare basalts suggests diverse mantle compositions and/or complex mantle dynamics. Taylor et al. suggested that  $\text{TiO}_2$  can be used to reflect the magma source region, with higher  $\text{TiO}_2$  content implying more primitive lunar mantle-derived magma (and vice versa for lunar crustal-derived magma) [43]. Mg-number ( $\text{Mg}^\# = \text{atomic Mg}/(\text{Mg} + \text{Fe})$ ) is an important petrologic discriminator for both terrestrial and lunar rocks [44] and can reflect the degree of basalt fractional crystallization.

In this study, we have calculated the average  $\text{TiO}_2$  and  $\text{Mg}^\#$  contents of the basalts from the margin of seven basins and the center of nine basins (Table S1, Figure 8). The basalts in the basin center and rim are named the Central Basin Basalt (CBB) and Rim Basin Basalt (RBB) in this paper, respectively (Figure 4d). The nine geological units of Mare Orientale belong to the CBB, while the seven geological units of Lacus Veris and Lacus Autumni belong to the RBB. Accordingly, the Mare Orientale basalts have higher  $\text{TiO}_2$  but lower  $\text{Mg}^\#$  contents than the Lacus Veris and Lacus Autumni basalts. The low-Ti magma was generated in the earlier stage, whilst the high-Ti magma was formed in the later stage [42].

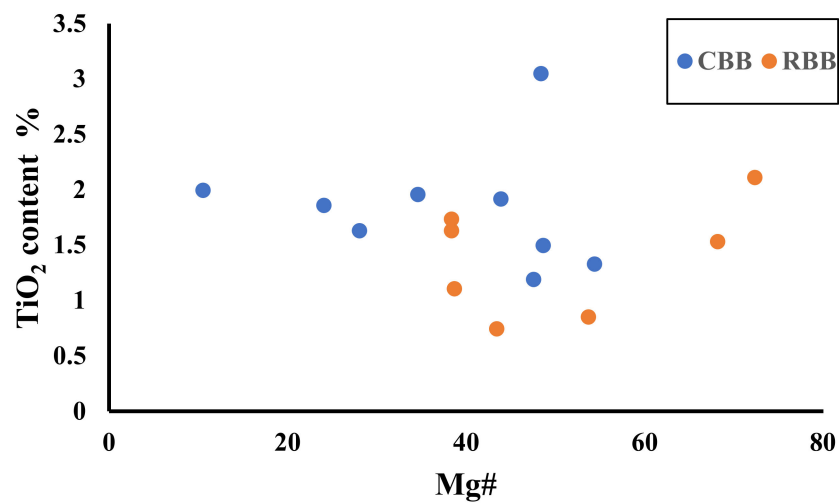


Figure 8. TiO<sub>2</sub> and Mg# content of the Orientale basalts.

This also shows that basalts in different regions may come from different sources: (1) if the basalts were sourced from other locations, the basalt composition on the basin margin should be similar to that in the center; (2) the basalt in the basin was likely formed from different stages and different source regions: basalt in the center is more fractionated and has a deeper source region, while that on the margin is less fractionated and has a shallower source region.

### 5.2.2. Relationship between Impact Direction and Basalt Distribution

The overall pattern of ejecta and offset mascon [45] indicates that the Orientale Basin was formed from an oblique impact. The focused stream spatial data analyzed using the LOLA DEM data can identify the ejecta patterns generated by oblique impacts [46] and the impact direction along a northeast-southwest line. Detailed ejecta facies of the Orientale Basin indicates the same northeast-southwest impact direction [46,47]. As shown in Figure 9, the line of bilateral symmetry is represented by the red line and the impact direction is indicated by the arrow at the southwestern end.

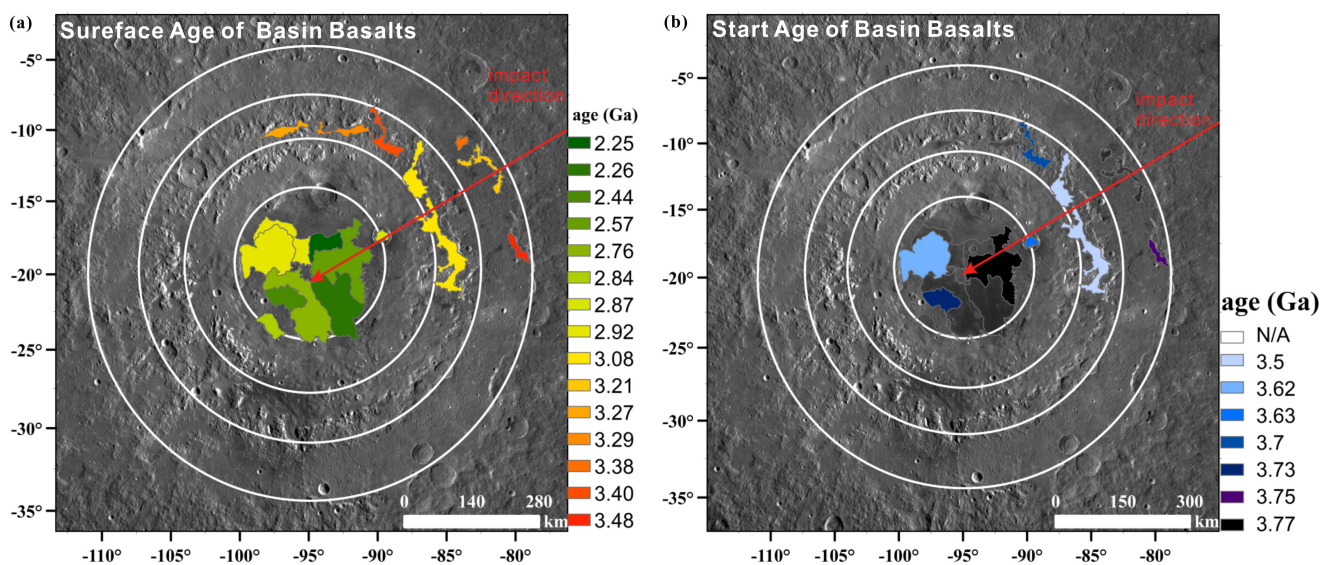


Figure 9. Relationship between impact direction and basalt distribution.

We found that there are much more basalts in the upstream than downstream of the Orientale impact direction, indicating that the basalt eruption occurred more likely toward the uprange. Combining the numerical simulation by Stickle et al. [48], the gravity gradient estimated by Andrews-Hanna et al. [49], and the findings on the Malt Wilson impact crater [50], we suggest that the impact occurred in the uprange and the center impact basin with more deep fractures, which led to the appearance of more basalt in the corresponding area.

### 5.2.3. Model for the Basin Volcanic Formation

Integrating our results and published works, we suggest that at 3.80 Ga, an impact body (50–80 km diameter) [51] may have struck the lunar surface obliquely forming the Orientale Basin [46,47]. The basin excavation process depressurized the underlying material and in-situ decompression melting occurred. Besides, more impact fractures were formed at the center and the upstream of the impact, forming a basin margin and alternating gravity gradients within the basin [49]. The mascon associated with the lunar maria may have created stress difference (~100 bar) within the upper 300 km of the lunar crust and mantle [52], and impact melting of the lunar mantle gradually formed a magma chamber. Approximately 30 My after the impact, the basalt may have erupted to the surface in the center. Due to the deeper faults in the upper reaches of the basin, some basalts may have erupted at the negative gravity anomalies upstream. Subsequently, the thermal energy caused by the impact continued to weaken, and the basalt eruption in the basin margin ceased. The thermal energy in the center and the gravity anomalies [52] may have continued the eruption for 1.51 Gy.

## 6. Conclusions

Based on the derived model ages, we conclude the following: (1) Both the central basalts and the margin basalts are characterized by multiple eruptions. The longest volcanism of the central basalt and margin basalt lasted for 1.51 and 0.67 Gy, respectively. The results provide a foundation to estimate the lunar basalt eruption rate and duration [53]; (2) spatial distribution of the basalts suggest that the basalt eruption occurred in the upstream and center of the Orientale impact tract and that there was almost no basalt eruption in the downstream of the tract; (3) the higher  $\text{TiO}_2$  and lower  $\text{Mg}^\#$  characteristics in the center basalt suggest that the continuous basalt eruption was sustained by the post-impact internal thermal evolution and gravity gradient changes. For future studies, it is necessary to verify whether such eruption pattern exists also in the volcanic formation of other basins. Meanwhile, numerical simulation of the volcanic formation can help to better understand it.

**Supplementary Materials:** The following supporting information can be downloaded at: <https://www.mdpi.com/article/10.3390/rs14061426/s1>, The craters counted in the different areas.scc; Figure S1: The division of geological units in previous papers; Table S1:  $\text{TiO}_2$  content and  $\text{Mg}^\#$  of the Orientale basalts. Refs [11,35,36,44] are cited in the supplementary materials.

**Author Contributions:** Conceptualization, J.L. (Jingwen Liu) and J.L. (Jianzhong Liu); methodology, J.L. (Jingwen Liu); software, J.L. (Jingwen Liu) and J.W.; validation, J.L. (Jingwen Liu) and J.W.; formal analysis, J.L. (Jingwen Liu); investigation, J.L. (Jingwen Liu); resources, J.L. (Jingwen Liu); data curation, J.L. (Jingwen Liu) and L.Z.; writing—original draft preparation, J.L. (Jingwen Liu); writing—review and editing, J.L. (Jingwen Liu) and J.L. (Jianzhong Liu); visualization, J.L. (Jingwen Liu) and K.Z.; supervision, J.L. (Jianzhong Liu); project administration, J.L. (Jianzhong Liu); funding acquisition, J.L. (Jianzhong Liu). All authors have read and agreed to the published version of the manuscript.

**Funding:** This work was supported by the Strategic Priority Research Program of the Chinese Academy of Sciences (Grant No. XDB 41000000), the Pre-research project on Civil Aerospace Technologies by CNSA (Grant No. D020201), the National Science and Technology Infrastructure Work Projects (Grant No. 2015FY210500), Beijing Municipal Science and Technology Commission (Grant No. Z181100002918003), the Key Program of Frontier Science of Chinese Academy of Sciences (Grant

No. QYZDY-SSW-DQC028), and the National Natural Science Foundation of China (Grant No. 41773065 and No. 41941003).

**Institutional Review Board Statement:** Not applicable.

**Informed Consent Statement:** Not applicable.

**Data Availability Statement:** The Chang'E series data (<http://moon.bao.ac.cn/>, accessed on 1 September 2019). The SLDEM2015 is available from LOLA Planetary Data System (PDS) Data Note (<http://imbrium.mit.edu/EXTRAS/>, accessed on 30 August 2020 SLDEM2015/). The LRO WAC images are available from the LRO data collections. ([https://astrogeology.usgs.gov/search/map/Moon/LRO/LROC\\_WAC/Lunar\\_LRO\\_LROC-WAC\\_Mosaic\\_global\\_100m\\_June2013](https://astrogeology.usgs.gov/search/map/Moon/LRO/LROC_WAC/Lunar_LRO_LROC-WAC_Mosaic_global_100m_June2013), accessed on 3 February 2020). The thorium abundance data are available from the PDS Geoscience Node ([https://pds-geosciences.wustl.edu/missions/lunarp/reduced\\_special.html](https://pds-geosciences.wustl.edu/missions/lunarp/reduced_special.html), accessed on 30 August 2020).

**Acknowledgments:** We gratefully acknowledge all those who worked on the Chang'E series data archive to make 7 m resolution CE-2 CCD s, the 20 m resolution CE-2 DTMs, and IIM data publicly available. We also thank the Planetary Data System archive for providing the LRO WAC imagery and SLDEM2015. We are grateful to the anonymous reviewers and editors for their constructive feedback, which improved the quality of this paper.

**Conflicts of Interest:** The authors declare no conflict of interest.

## References

- Moriarty, D.P., 3rd; Dygert, N.; Valencia, S.N.; Watkins, R.N.; Petro, N.E. The search for lunar mantle rocks exposed on the surface of the Moon. *Nat. Commun.* **2021**, *12*, 4659. [[CrossRef](#)] [[PubMed](#)]
- Kruijjer, T.S.; Kleine, T. Tungsten isotopes and the origin of the Moon. *Earth Planet. Sci. Lett.* **2017**, *475*, 15–24. [[CrossRef](#)]
- Ziethe, R.; Seiferlin, K.; Hiesinger, H. Duration and extent of lunar volcanism: Comparison of 3D convection models to mare basalt ages. *Planet. Space Sci.* **2009**, *57*, 784–796. [[CrossRef](#)]
- Dygert, N.; Hirth, G.; Liang, Y. A flow law for ilmenite in dislocation creep: Implications for lunar cumulate mantle overturn. *Geophys. Res. Lett.* **2016**, *43*, 532–540. [[CrossRef](#)]
- Hess, P.C.; Parmentier, E. A model for the thermal and chemical evolution of the Moon's interior: Implications for the onset of mare volcanism. *Earth Planet. Sci. Lett.* **1995**, *134*, 501–514. [[CrossRef](#)]
- Hiesinger, H.; Jaumann, R.; Neukum, G.; Head, J.W. Ages of mare basalts on the lunar nearside. *J. Geophys. Res. Planets* **2000**, *105*, 29239–29275. [[CrossRef](#)]
- Hiesinger, H.; Head, J.W.; Wolf, U.; Jaumann, R.; Neukum, G. Ages and stratigraphy of lunar mare basalts in Mare Frigoris and other nearside maria based on crater size-frequency distribution measurements. *J. Geophys. Res. Planets* **2010**, *115*, 1–22. [[CrossRef](#)]
- Hiesinger, H.; Head, J.W.; Wolf, U.; Jaumann, R.; Neukum, G. Ages and stratigraphy of mare basalts in Oceanus Procellarum, Mare Nubium, Mare Cognitum, and Mare Insularum. *J. Geophys. Res. Planets* **2003**, *108*, 1–27. [[CrossRef](#)]
- Hiesinger, H.; Head, J.; Wolf, U.; Jaumann, R.; Neukum, G.; Advances, J.R. Ages and stratigraphy of lunar mare basalts: A synthesis. *Lunar Stratigr.* **2011**, *477*, 1–51. [[CrossRef](#)]
- Morota, T.; Haruyama, J.; Ohtake, M.; Matsunaga, T.; Honda, C.; Yokota, Y.; Kimura, J.; Ogawa, Y.; Hirata, N.; Demura, H.; et al. Timing and characteristics of the latest mare eruption on the Moon. *Earth Planet. Sci. Lett.* **2011**, *302*, 255–266. [[CrossRef](#)]
- Lucey, P.G.; Blewett, D.T.; Hawke, B.R. Mapping the FeO and TiO<sub>2</sub> content of the lunar surface multispectral imagery. *J. Geophys. Res. Planets* **1998**, *103*, 3679–3699. [[CrossRef](#)]
- Pasckert, J.H.; Hiesinger, H.; van der Bogert, C.H. Lunar farside volcanism in and around the South Pole–Aitken basin. *Icarus* **2018**, *299*, 538–562. [[CrossRef](#)]
- Head, J.W.; Wilson, L. Lunar Mare Volcanism: Stratigraphy, Eruption Conditions, and the Evolution of Secondary Crusts. *Geochim. Cosmochim. Acta* **1992**, *56*, 2155–2175. [[CrossRef](#)]
- Head, J.W.; Hawke, B.R. Geology of the Apollo 14 region/Fra Mauro/-Stratigraphic history and sample provenance. In Proceedings of the 6th Lunar Science Conference, Houston, TX, USA, 17–21 March 1975; Volume 6, pp. 2483–2501.
- Arivazhagan, S. Quantitative Characterization of lunar Mare Orientale basalts detected by moon mineralogical mapper on Chandrayaan-1. In *Planetary Exploration and Science: Recent Results and Advances*; Springer: Berlin/Heidelberg, Germany, 2015; pp. 21–43.
- Jolliff, B.L.; Gillis, J.J.; Haskin, L.A.; Korotev, R.L.; Wieczorek, M.A. Major lunar crustal terranes: Surface expressions and crust-mantle origins. *J. Geophys. Res. Planets* **2000**, *105*, 4197–4216. [[CrossRef](#)]
- Liu, J.; Liu, J.; Yue, Z.; Zhang, L.; Wang, J.; Zhu, K. Characterization and interpretation of the global lunar impact basins based on remote sensing. *Icarus* **2022**, *378*, 114952. [[CrossRef](#)]
- Baldwin, R.B. Summary of arguments for a hot moon. *Science* **1970**, *170*, 1297–1300. [[CrossRef](#)] [[PubMed](#)]
- Arkani-Hamed, J. On the thermal history of the moon. *Moon* **1973**, *6*, 380–383. [[CrossRef](#)]

20. Whitten, J.; Head, J.W.; Staid, M.; Pieters, C.M.; Mustard, J.; Clark, R.; Nettles, J.; Klima, R.L.; Taylor, L. Lunar mare deposits associated with the Orientale impact basin: New insights into mineralogy, history, mode of emplacement, and relation to Orientale Basin evolution from Moon Mineralogy Mapper (M3) data from Chandrayaan-1. *J. Geophys. Res. Planets* **2011**, *116*, E00G09. [[CrossRef](#)]
21. Yue, Z.; Yang, M.; Jia, M.; Michael, G.; Di, K.; Gou, S.; Liu, J. Refined model age for Orientale Basin derived from zonal crater dating of its ejecta. *Icarus* **2020**, *346*, 113804. [[CrossRef](#)]
22. Nahm, A.L.; Ohman, T.; Kring, D.A. Normal faulting origin for the Cordillera and Outer Rook Rings of Orientale Basin, the Moon. *J. Geophys. Res. Planets* **2013**, *118*, 190–205. [[CrossRef](#)]
23. Wilhelms, D.E.; John, F.; Trask, N.J. *The Geologic History of the Moon*; United States Government Publishing Office: Washington, DC, USA, 1987; pp. 2330–7102. [[CrossRef](#)]
24. Neukum, G.; König, B.; Arkan-Hamed, J. A study of lunar impact crater size-distributions. *Moon* **1975**, *12*, 201–229. [[CrossRef](#)]
25. Baldwin, R.B. On the Relative and Absolute Ages of 7 Lunar Front Face Basins: II. From Crater Counts. *Icarus* **1987**, *71*, 19–29. [[CrossRef](#)]
26. Greeley, R. Modes of emplacement of basalt terrains and an analysis of mare volcanism in the Orientale Basin. In Proceedings of the Lunar and Planetary Science Conference Proceedings, Houston, TX, USA, 15–19 March 1976; pp. 2747–2759.
27. Greeley, R.; Kadel, S.D.; Williams, D.A.; Gaddis, L.R.; Head, J.W.; McEwen, A.S.; Murchie, S.L.; Nagel, E.; Neukum, G.; Pieters, C.M.; et al. Galileo imaging observations of lunar maria and related deposits. *J. Geophys. Res. Planets* **1993**, *98*, 17183–17205. [[CrossRef](#)]
28. Cho, Y.; Morota, T.; Haruyama, J.; Yasui, M.; Hirata, N.; Sugita, S. Young mare volcanism in the Orientale region contemporary with the Procellarum KREEP Terrane (PKT) volcanism peak period ~2 billion years ago. *Geophys. Res. Lett.* **2012**, *39*, 1–5. [[CrossRef](#)]
29. Kneissl, T.; van Gasselt, S.; Neukum, G. Map-projection-independent crater size-frequency determination in GIS environments—New software tool for ArcGIS. *Planet. Space Sci.* **2011**, *59*, 1243–1254. [[CrossRef](#)]
30. Michael, G.; Neukum, G. Planetary surface dating from crater size–frequency distribution measurements: Partial resurfacing events and statistical age uncertainty. *Earth Planet. Sci. Lett.* **2010**, *294*, 223–229. [[CrossRef](#)]
31. Pike, R.J. *Geometric Interpretation of Lunar Craters*; U.S. Government Printing Office: Washington, DC, USA, 1980.
32. Oberbeck, V.R.; Morrison, R.H. Laboratory simulation of the herringbone pattern associated with lunar secondary crater chains. *Moon* **1974**, *9*, 415–455. [[CrossRef](#)]
33. Melosh, H.J. *Impact Cratering: A Geologic Process*; Oxford University Press: New York, NY, USA, 1989.
34. Zuo, W.; Li, C.; Zhang, Z. Scientific data and their release of Chang’E-1 and Chang’E-2. *Chin. J. Geochem.* **2014**, *33*, 24–44. [[CrossRef](#)]
35. Wu, Y.; Xue, B.; Zhao, B.; Lucey, P.; Chen, J.; Xu, X.; Li, C.; Ouyang, Z. Global estimates of lunar iron and titanium contents from the Chang’E-1 IIM data. *J. Geophys. Res. Planets* **2012**, *117*, 1–23. [[CrossRef](#)]
36. Prettyman, T.H.; Hagerty, J.J.; Elphic, R.C.; Feldman, W.C.; Lawrence, D.J.; McKinney, G.W.; Vaniman, D.T. Elemental composition of the lunar surface: Analysis of gamma ray spectroscopy data from Lunar Prospector. *J. Geophys. Res. Planets* **2006**, *111*, 1–41. [[CrossRef](#)]
37. Morota, J.; Ohtake, M.; Matsunaga, T.; Yokota, Y.; Honda, C.; Sugihara, T.; Kimura, J.; Ishihara, Y. Mare Volcanism on the Farside and in the Orientale Region of the Moon. In Proceedings of the 41st Lunar and Planetary Science Conference, The Woodlands, TX, USA, 1–5 March 2010; p. 1309.
38. Spudis, P.D.; Martin, D.J.; Kramer, G. Geology and composition of the Orientale basin impact melt sheet. *J. Geophys. Res. Planets* **2014**, *119*, 19–29. [[CrossRef](#)]
39. Kodama, S.; Yamaguchi, Y. Lunar mare volcanism in the eastern nearside region derived from Clementine UV/VIS data. *Meteorit. Planet. Sci.* **2003**, *38*, 1461–1484. [[CrossRef](#)]
40. Hiesinger, H.; Jaumann, R.; Neukum, G.; Head, J. On the relation of age and titanium content of lunar mare basalts. In Proceedings of the 29th Annual Lunar and Planetary Science Conference, Houston, TX, USA, 16–20 March 1998; p. 1243.
41. Hiesinger, H.; Head, J.; Wolf, U.; Neukum, G. Lunar mare basalts: Mineralogical variations with time. In Proceedings of the 32nd Lunar and Planetary Science Conference, Houston, TX, USA, 12–16 March 2001; p. 1826.
42. Kodama, S.; Yamaguchi, Y. Mare volcanism on the Moon inferred from Clementine UVVIS data. In Proceedings of the 36th Annual Lunar and Planetary Science Conference, League City, TX, USA, 14–18 March 2005; p. 1641.
43. Taylor, G.J.; Warren, P.; Ryder, G.; Delano, J.; Pieters, C.; Lofgren, G. Lunar rocks. In *Lunar Sourcebook*; Cambridge University Press: Cambridge, UK, 1991; pp. 183–284.
44. Cahill, J.; Lucey, P.; Gillis, J.; Steutel, D. Global Mapping of Mg-Number Derived from Clementine Data. In *AGU Fall Meeting Abstracts*; American Geophysical Union: San Francisco, CA, USA, 17 December 2004; p. P23A-0232.
45. Schultz, P. Making the man in the moon: Origin of the Imbrium Basin. In Proceedings of the Twenty-sixth Lunar and Planetary Science Conference, Houston, TX, USA, 13–17 March 1995; pp. 1251–1252.
46. Liu, J.W.; Liu, J.Z.; Guo, D.J.; Ji, J.Z.; Wang, Q.L.; Li, S.J. Comprehensive analysis of the lunar Orientale Basin and research of the initial impact condition. *Acta Petrol. Sin.* **2016**, *32*, 135–143.
47. Morse, Z.R.; Osinski, G.R.; Tornabene, L.L. New morphological mapping and interpretation of ejecta deposits from Orientale Basin on the Moon. *Icarus* **2018**, *299*, 253–271. [[CrossRef](#)]

48. Stickle, A.; Schultz, P. Investigating pressure magnitudes at depth for oblique impacts into layered targets: Applications to terrestrial impacts in sedimentary targets. *Meteorit. Planet. Sci.* **2013**, *48*, 1638–1650. [[CrossRef](#)]
49. Andrews-Hanna, J.C.; Head, J.W.; Johnson, B.; Keane, J.T.; Kiefer, W.S.; McGovern, P.J.; Neumann, G.A.; Wieczorek, M.A.; Zuber, M.T. Ring faults and ring dikes around the Orientale basin on the Moon. *Icarus* **2018**, *310*, 1–20. [[CrossRef](#)]
50. Kenkmann, T.; Poelchau, M.H. Low-angle collision with Earth: The elliptical impact crater Matt Wilson, Northern Territory, Australia. *Geology* **2009**, *37*, 459–462. [[CrossRef](#)]
51. Potter, R.W.; Kring, D.A.; Collins, G.S.; Kiefer, W.S.; McGovern, P.J. Numerical modeling of the formation and structure of the Orientale impact basin. *J. Geophys. Res. Planets* **2013**, *118*, 963–979. [[CrossRef](#)]
52. Arkani-Hamed, J. Effect of a giant impact on the thermal evolution of the Moon. *Moon* **1974**, *9*, 183–209. [[CrossRef](#)]
53. Head, J.W. Lava Flooding of Ancient Planetary Crusts—Geometry, Thickness, and Volumes of Flooded Lunar Impact Basins. *Moon Planets* **1982**, *26*, 61–88. [[CrossRef](#)]